J.-S. Lönnroth, V. Parail, V. Hynönen, T. Johnson, T. Kiviniemi, N. Oyama, M. Beurskens, D. Howell, G. Saibene, P. de Vries, T. Hatae, Y. Kamada, S. Konovalov, A. Loarte, K. Shinohara, K. Tobita, H. Urano, and JET EFDA contributors. 2007. Effects of ripple-induced ion thermal transport on H-mode plasma performance. Plasma Physics and Controlled Fusion, volume 49, number 3, pages 273-295.

http://www.iop.org/journals/ppcf
http://stacks.iop.org/ppcf/49/273

INSTITUTE OF PHYSICS PUBLISHING PLASMA PHYSICS AND CONTROLLED FUSION

Plasma Phys. Control. Fusion **49** (2007) 273–295 doi:10.1088/0741-3335/49/3/007

Effects of ripple-induced ion thermal transport on H-mode plasma performance

J-S Lönnroth[1], V Parail[2], V Hynönen[1], T Johnson[3], T Kiviniemi[1], N Oyama[4], M Beurskens[2], D Howell[2], G Saibene[5], P de Vries[2], T Hatae[4], Y Kamada[4], S Konovalov[4], A Loarte[5], K Shinohara[4], K Tobita[4], H Urano[4] and JET EFDA contributors[6]

[1] Association EURATOM-Tekes, Helsinki University of Technology, PO Box 4100, 02015 HUT, Finland
[2] EURATOM/UKAEA Fusion Association, Culham Science Centre, Abingdon, Oxfordshire OX14 3DB, UK
[3] Association EURATOM-VR, Alfvén Laboratory, Royal Institute of Technology, 10044 Stockholm, Sweden
[4] Japan Atomic Energy Agency, Naka, Ibaraki-ken, 311-0193, Japan
[5] EFDA Close Support Unit, c/o Max Planck Institut für Plasmaphysik, Boltzmannstrasse 2, 85748 Garching, Germany

Received 12 May 2006, in final form 28 November 2006
Published 15 February 2007
Online at stacks.iop.org/PPCF/49/273

Abstract

A recent series of dimensionless pedestal identity experiments at JET and JT-60U failed to produce a match in the dimensional pedestal parameters and edge-localized mode (ELM) frequency despite a good match in the main dimensionless plasma parameters. This paper describes the progress made in understanding these experimental results. First, it is investigated whether differences in the magnetohydrodynamic stability of the pedestal, including those potentially arising from the 10% difference in the aspect ratio between the two tokamaks, can explain the results. The potential effects of differences in plasma rotation between the two machines are also examined. Given the result that these mechanisms fail to explain the experimental observations and the fact that JT-60U features considerably stronger toroidal magnetic field ripple than JET, the bulk of the paper, however, discusses the effects of ripple losses. The analysis shows that ripple losses of thermal ions can affect H-mode plasma performance very sensitively. Orbit-following simulations indicate that losses due to diffusive transport give rise to a wide radial distribution of enhanced ion thermal transport, whereas non-diffusive losses have a very edge-localized distribution. In predictive transport simulations with an energy sink term in the continuity equation for the ion pressure representing non-diffusive losses, reduced performance as well as an increase in the ELM

[6] See appendix of Paméla J *et al* 2004 *Proc. 20th Int. Conf. on Fusion Energy 2004 (Vilamoura 2004)* (Vienna: IAEA).

frequency are demonstrated. This indicates that non-diffusive losses might play an important role in determining the performance and ELM properties of JT-60U plasmas. Interestingly, the result also suggests that ripple losses could be used as a tool for ELM mitigation in future tokamaks. In simulations with a wide radial distribution of enhanced ion thermal transport consistent with what would be attributable to losses due to diffusive transport, an improvement in confinement and a reduction in the ELM frequency are observed, a result resembling experimental observations for low ripple amplitudes in previous JET ripple experiments. This indicates that ripple losses need not always have a detrimental influence on plasma performance.

(Some figures in this article are in colour only in the electronic version)

1. Introduction

The high confinement mode (H-mode) offers a promising regime for tokamak operation. H-mode plasmas are characterized by the formation of an edge transport barrier (ETB), a thin layer with suppressed anomalous transport just inside the magnetic separatrix, resulting in a steep edge pressure gradient and improved confinement. The ETB generally features strong periodic bursts of particles and energy, referred to as edge-localized modes (ELMs), which limit the achievable level of pressure gradient [1,2]. In addition to that, ELMs have the disadvantage of causing large peak heat loads on the divertor plates, which can be a serious problem in large tokamaks. On the other hand, ELMs also have the beneficial effect of transporting impurities across the pedestal region, thus helping to prevent the plasma from terminating due to impurity accumulation. Recently, a variety of studies on ELMy H-modes have been carried out at the JET and JT-60U tokamaks discussed in this paper. See, e.g. [3,4]. ELMs are believed to be controlled by a combination of magnetohydrodynamic (MHD) ballooning mode instabilities, controlled mainly by the edge pressure gradient, and kink/peeling mode instabilities, driven mainly by the edge current. Given the importance of achieving good plasma confinement and the role played by ELMs in relation to this goal, much effort has been put into understanding and predicting how confinement and ELM properties depend on various plasma parameters, which has led to the development of various scaling laws [5–7]. A interesting application is to test such dependences in identity experiments between two or more tokamaks.

The dimensionless identity technique makes use of the invariance of plasma physics to changes in the dimensional plasma parameters. Recently, a series of dimensionless pedestal identity experiments has been carried out at JET and JT-60U [8]. In these experiments, a good match was obtained in all the main dimensionless plasma parameters, normalized plasma pressure β, Larmor radius ρ^* and collisionality ν^*. A special JT-60U-like equilibrium was developed at JET in order to match the triangularity δ and elongation κ of JT-60U. In comparison with dimensionless pedestal identity experiments carried out between JET and other tokamaks such as ASDEX Upgrade and DIII-D, the JET/JT-60U identity is of special interest, because the similar size of the two machines makes it possible to carry out dimensionless pedestal identity experiments between them with very similar dimensional parameters. Only the inverse aspect ratio ϵ cannot be matched very closely at the two machines due to the slightly larger major radius at JT-60U. Specifically, $\epsilon = 0.29$ has been used at JET and $\epsilon = 0.25$ at JT-60U in the recent experiments.

Despite the good match in dimensionless parameters, the pedestal identity experiments failed to produce plasmas with similar dimensional pedestal parameters. Specifically, the ELM

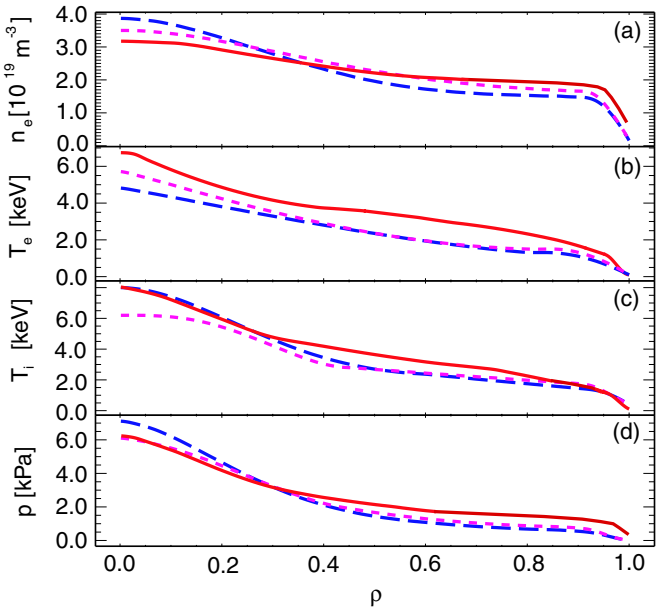

Figure 1. Radial profiles of (*a*) electron density, (*b*) electron temperature, (*c*) ion temperature and (*d*) total pressure in JET discharge 60856 (——) and the PNB phase (— — —) and PNB + NNB phase (– – –) of the best-matching JT-60U discharge E43075. The profiles shown here are smoothed fits to experimental data.

frequency is generally lower and the pedestal performance better in the JET discharges than in their JT-60U matches. A detailed description of the first results of the dimensionless pedestal identity experiments at JET and JT-60U can be found in [8]. The present paper describes the highlights of a systematic research effort with the aim of improving the understanding of the observed discrepancies. To begin with, it is investigated whether the observed differences in the ELM frequency and pedestal performance between JET and JT-60U can be explained by differences in the linear MHD stability of the pedestal including effects due to a slight difference in the aspect ratio and significant differences in toroidal plasma rotation between the two machines. The rest of the paper then discusses the effects of ripple-induced thermal ion losses on H-mode plasma performance, the rationale for this being that JT-60U features significantly stronger toroidal magnetic field ripple than JET and that even a small level of additional ion thermal transport may have a profound impact on the pedestal performance and ELMs.

2. Linear MHD stability analysis

Differences in the MHD stability of the pedestal were initially proposed as a possible explanation for the discrepancies between JET and JT-60U in the dimensionless pedestal identity experiments. Some typical results of the initial ideal linear MHD stability analysis are presented in the following. A representative pair of JET/JT-60U identity plasmas have been selected for the discussion, JET discharge 60856 and the matching JT-60U discharge E43075. These are discharges with low plasma current ($I_p = 1.1$ MA) and relatively high toroidal magnetic field ($B_t = 1.8$ T on the magnetic axis in the case of JET and $B_t = 1.9$ T in the case of JT-60U). Figure 1 shows the electron density, electron and ion temperature and total

thermal pressure profiles (smoothed fits to experimental data) for the two discharges. The fast ion contribution from the neutral beam sources has not been included in the pressure profiles used in MHD stability analysis, because it is negligible in the edge plasma, the properties of which define edge MHD stability. The effect of impurities is taken into account by using an appropriately chosen effective charge number to scale the ion density profile.

In the case of the JT-60U plasma, there are two slightly different profiles in each plot from the different phases of the discharge in figure 1. The pulse has a phase with positive ion neutral beam heating (PNB) followed by a phase with a combination of roughly equal amounts of absorbed power from PNB and negative ion neutral beam heating (NNB). The two sets of JT-60U plasma profiles correspond to these two phases. It should be noted that the average beam energies and therefore beam-injected currents are rather different during the PNB and PNB+NNB phases. For PNB, the average beam energy is 86 keV, whereas for NNB it is 370 keV. The beam-driven current is around 0.17 MA during the PNB phase and around 0.51 MA during the combined phase.

The plasma profiles in figure 1 have been reconstructed by interpolating and smoothing out the experimental data, as shown in figures 2–4. Figure 2 shows the electron temperature, the ion temperature and the electron density data from a variety of diagnostics for the JET discharge together with the fits used in the MHD stability calculations (and in figure 1). For clarity, the uncertainties of the experimental data points in figure 2 are summarized separately in table 1. Figures 3 and 4 show similar plots for the PNB and PNB+NNB phases of the JT-60U discharge. The error bars of each experimental data point are indicated in the figure. The fits to the experimental profile data have been used in interpretative transport simulations, which have subsequently been used as input for the ideal linear MHD stability analysis. The pressure profile in figure 1 follows from the density and temperature profiles. It should be noted that the pedestal pressure is significantly higher in JET than in JT-60U due to the higher density at JET. Because of profile stiffness this also translates into higher core pressure at JET. In the deep core, however, the JT-60U discharge features a weak ITB [9], which leads to a steep pressure gradient in the region from around $\rho = 0.4$ to the centre, visible as a change in the slope in the profile plots, and thus to an improved overall confinement.

Figure 5 illustrates the results of MHD stability analysis with the MHD equilibrium solver HELENA and the ideal linear MHD stability code MISHKA-1 [10]. Shown in the figure are MHD stability diagrams corresponding to the three sets of plasma profiles shown in figure 1, i.e. for JET discharge 60856 and both heating phases of JT-60U discharge E43075. The diagrams indicate the toroidal mode numbers of the most unstable kink, peeling or ballooning modes ($n \leqslant 14$) at a number of locations in the operational space defined by the normalized pressure gradient $\alpha = -(2\mu_0 q^2 \epsilon / B_t^2)(\mathrm{d}p/\mathrm{d}\rho)$ and magnetic shear s, as well as the infinite n ballooning unstable region and the operational point. Here, q is the safety factor, p is the pressure and ρ is the square root of the normalized toroidal flux. The plots roughly correspond to the flux surface with the largest pressure gradient, $\rho = 0.98$ for the JET discharge and $\rho = 0.95$ for the JT-60U discharge. A comparison of the three plots shows that they are qualitatively similar. In each case, the discharge enters the second ballooning stability region. Obviously, the plasma enters deeper into the second stability and hits the finite n ballooning stability limit in the case of JET. There is no clear explanation for why the operational point does not reach the finite n ballooning stability limit in the case of the JT-60U discharge, due to which the pressure gradient remains lower than at JET. It should also be noted that for reasons not yet fully understood the performance is better in the combined heating phase than in the PNB phase of the JT-60U discharge, which is a typical result for discharges with low plasma current.

The result illustrated by figure 5 is fairly general. A large number of JET and JT-60U pedestal identity plasmas were analysed, but the analysis failed to show any general qualitative

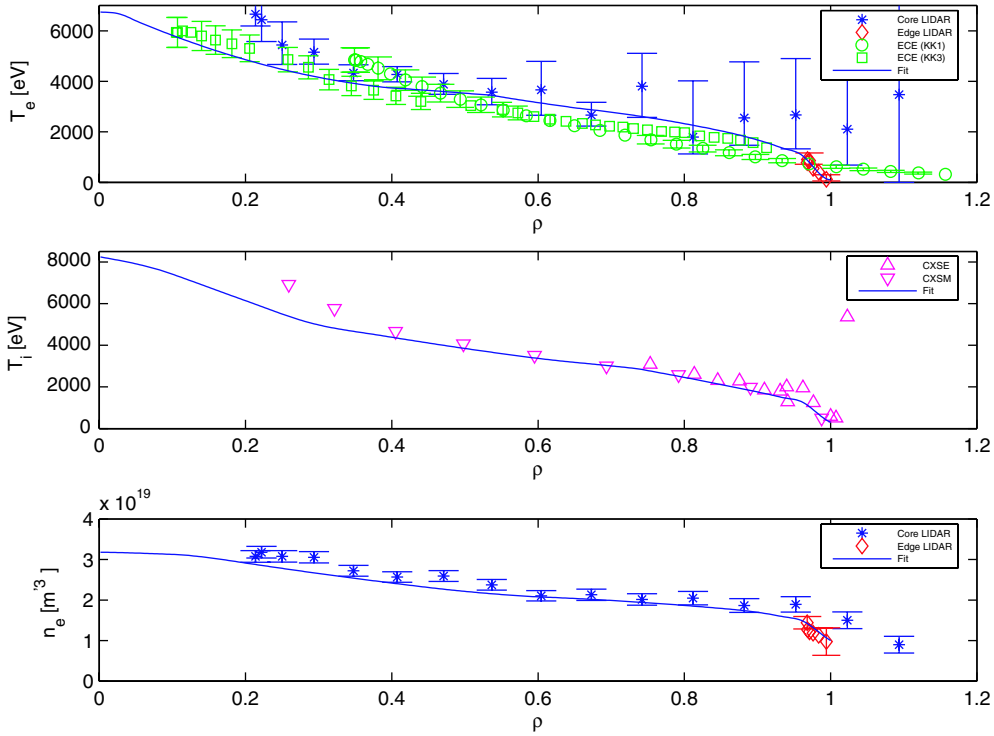

Figure 2. Experimental data and fits to it (also shown in figure 1) for JET discharge 60856. (*a*) Electron temperature data (core LIDAR (Thomson scattering) data, edge LIDAR (Thomson scattering) data and electron cyclotron emission spectroscopy data (diagnostics known as KK1 and KK3)) and fit. (*b*) Ion temperature data (charge exchange recombination spectroscopy data (diagnostics known as CXSM and CXSE)) and fit. (*c*) Electron density data (core LIDAR (Thomson scattering) data and edge LIDAR (Thomson scattering) data) and fit. For clarity, error bars are generally shown in the figure only where they are larger than the actual datapoints and where they do not overlap too much with other datapoints or error bars. In particular, the validated uncertainty ranges for the charge exchange recombination spectroscopy data points are too small to be shown in a meaningful way. In order to shed some more light on the uncertainty ranges for the various types of diagnostic data used in the figure, the (vertical) uncertainty ranges of the experimental data points are summarized separately in table 1. It should also be noted that in order to correct for the inability of the diagnostic system to correctly localize the separatrix, the edge LIDAR raw data points have been shifted outwards by 2.5 cm (in real space, corresponding to a shift of 0.05 in ρ space) according to a standard procedure, so that they line up properly with other diagnostics, whose position calibration is known.

differences in the MHD stability between the two machines. Something like a clear failure to access second stability in the case of JT-60U plasmas could have explained the lower pedestal height and higher ELM frequency at this machine, but this was never observed. The conclusion of the analysis is, therefore, that the discrepancies in pedestal performance and ELM frequency between JET and JT-60U cannot be explained by differences in the ideal linear MHD stability of the pedestal.

Because of the mismatch of around 10% in the aspect ratio between JET and JT-60U, the explicit dependence of the MHD stability of the pedestal on the aspect ratio was also studied separately. This was done by artificially varying the aspect ratio in a JET discharge, pulse 59219 from the JT-60U identity series, thus eliminating all other effects that may potentially have

Table 1. Summary of the vertical uncertainties of the experimental data points of JET discharge 60856 in figure 2. The table gives some statistics about the uncertainty ranges for the data points associated with each diagnostic used in figure 2: Thomson scattering (diagnostics known as core and edge LIDAR), electron cyclotron emission spectroscopy (diagnostics known as KK1 and KK3) and charge exchange recombination spectroscopy (diagnostics known as CXSE and CXSM). For each diagnostic, the following statistics are given: the average, medium and largest single distance from the actual data points to the lower and upper bounds, respectively, of the uncertainty ranges of the data points.

Diagnostic	Mean deviation to lower bound	Median deviation to lower bound	Maximum deviation to lower bound	Mean deviation to upper bound	Median deviation to upper bound	Maximum deviation to upper bound	Unit
Core LIDAR, T_e	1.00	0.63	3.76	2.98	0.69	4.76	keV
Edge LIDAR, T_e	0.20	0.21	0.32	0.29	0.29	0.44	keV
ECE (KK1), T_e	0.29	0.29	0.48	0.29	0.29	0.48	keV
ECE (KK3), T_e	0.40	0.40	0.60	0.40	0.40	0.60	keV
CXSE, T_i	0.15	0.08	1.08	0.15	0.08	1.08	keV
CXSM, T_i	0.04	0.03	0.12	0.04	0.03	0.12	keV
Core LIDAR, n_e	0.16	0.15	0.31	0.16	0.15	0.31	10^{19} m^{-3}
Edge LIDAR, n_e	0.17	0.15	0.34	0.17	0.15	0.34	10^{19} m^{-3}

hidden the effect of the aspect ratio in the initial analysis. By shifting the plasma boundary outwards by 20 cm and 40 cm, the inverse aspect ratio was reduced from the original $\epsilon = 0.29$ to $\epsilon = 0.27$ and $\epsilon = 0.25$, respectively. The results of this analysis are summarized in the three MHD stability diagrams in figure 6 corresponding to $\epsilon = 0.29$, $\epsilon = 0.27$ and $\epsilon = 0.25$, respectively (see also [8]). Qualitatively, the three diagrams are very similar, but the operational α decreases with decreasing inverse aspect ratio. The change in α comes from the dependence of α on the aspect ratio, $\alpha \sim \epsilon$, and not from changes in the pressure gradient $\mathrm{d}p/\mathrm{d}\rho$. In fact, the pressure gradient, $\mathrm{d}p/\mathrm{d}\rho$, remains almost unchanged in the three cases. The results indicate that the dependence on the aspect ratio is fairly weak and cannot account for the large difference in the pedestal pressure found experimentally between JET and JT-60U.

The explicit effect of toroidal rotation was also studied separately. As described in [8], there are significant differences in plasma rotation in the similarity plasmas produced at JET and JT-60U. In particular, JET plasmas co-rotate, whereas JT-60U plasmas counter-rotate and generally feature a lower rotation velocity than JET plasmas. An advanced version of the MISHKA code, MISHKA-D-FLOW [11], was used to study the effect of plasma rotation on linear MHD stability. This version of the code takes into account the stabilizing effect of the ion diamagnetic drift as well as first order effects due to rotation, i.e. shear of rotation. The analysis shows that plasma rotation plays only a marginal role in the MHD stability of the pedestal. When a realistic rotation profile is imposed, the code typically gives a growth rate less than 1% smaller than without rotation. From this it follows that taking rotation into account results in very little change in the α–s MHD stability diagrams. This result is in agreement with the most recent analysis of experimental data, which shows that imposing toroidal rotation in JT-60U has a rather small effect on the pedestal pressure [12]. Taking the stabilizing effect of the ion diamagnetic drift into account does lead to some changes in the stability diagrams, mainly in the form of certain modes being stabilized completely in comparison with the MISHKA-1 result, but again the effect is not dramatic and does not affect the overall stability situation qualitatively. The conclusion is that although they play some role and affect plasma behaviour to some extent [13], the differences in rotation alone do not seem to be enough to account for the observed discrepancies in pedestal performance and ELM frequency between the two machines.

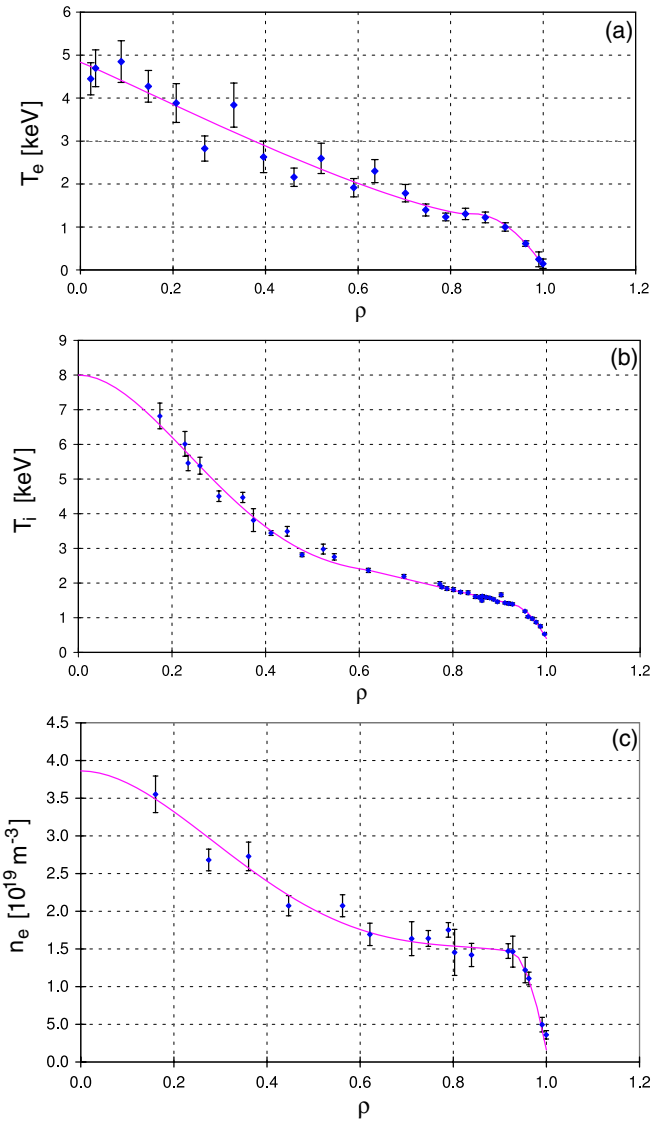

Figure 3. Experimental data and fits to it (also shown in figure 1) for the PNB phase ($t = 5.5$ s) of JT-60U discharge 60856. (*a*) Electron temperature data (Thomson scattering data) with error bars and fit. (*b*) Ion temperature data (charge exchange recombination spectroscopy data) with error bars and fit. (*c*) Electron density data (Thomson scattering data) with error bars and fit.

3. Ripple losses

The discreteness of the toroidal magnetic field coil configuration in tokamaks shows up as a ripple in the toroidal magnetic field, which results in ripple losses of both thermal and fast ions. The effects of ripple-induced fast ion losses have been investigated in several studies, both experimentally and theoretically, and on several machines [12, 14–18]. Until recently, ripple transport due to thermal ion losses has been relatively unexplored, despite its potential importance for the performance of tokamak plasmas. This lack of interest can at least in part

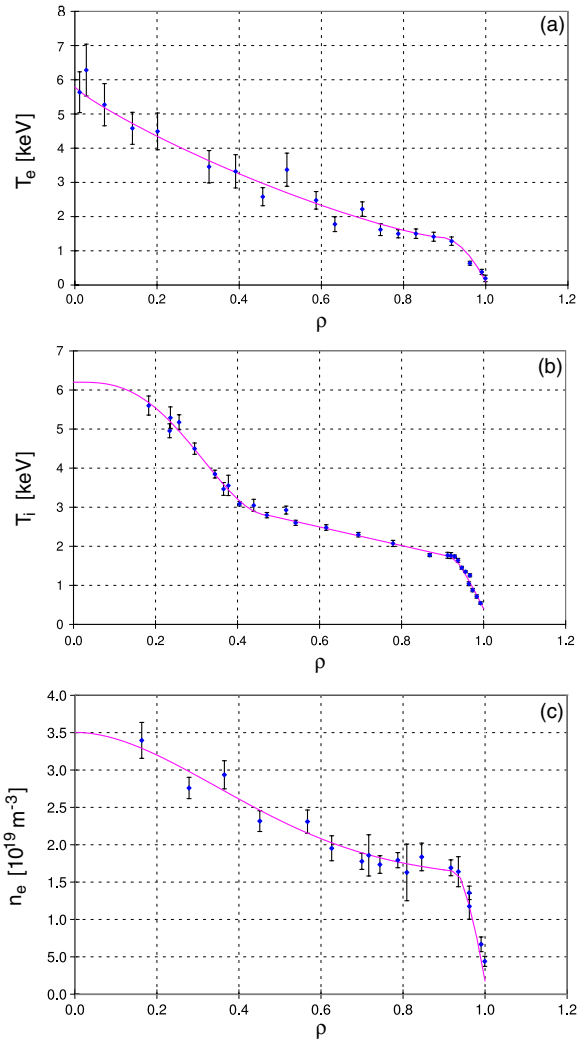

Figure 4. Experimental data and fits to it (also shown in figure 1) for the PNB+NNB phase ($t = 8.5$ s) of JT-60U discharge 60856. (*a*) Electron temperature data (Thomson scattering data) with error bars and fit. (*b*) Ion temperature data (charge exchange recombination spectroscopy data) with error bars and fit. (*c*) Electron density data (Thomson scattering data) with error bars and fit.

be attributed to associations with L-mode transport. In the L-mode, all transport coefficients have relatively large values in the region just inside the separatrix, in comparison with which any ripple-induced additional transport is small in magnitude. Any effects due to the ripple field will therefore be completely hidden behind the normal L-mode physics. In the H-mode, things are different. Transport in the ETB is suppressed to a very low level, whereby the effects of any additional ripple-induced transport can be very discernible.

The rationale for exploring the effect of ripple losses in the context of the JET/JT-60U pedestal identity experiments is that JT-60U features a high level of toroidal magnetic field ripple in comparison with JET. Specifically, JT-60U can operate with a ripple amplitude of up to 3% at the outer midplane separatrix, whereas JET normally operates at about 0.1%.

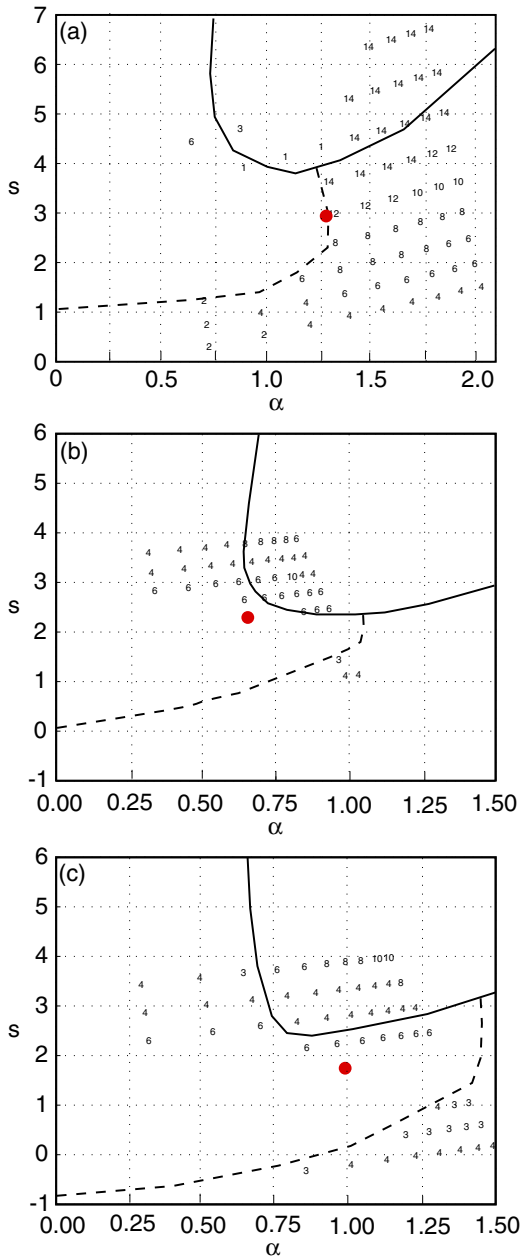

Figure 5. MHD stability diagrams corresponding to the three sets of plasma profiles shown in figure 1. (*a*) JET discharge 60856, $\rho = 0.98$. (*b*) The PNB phase of JT-60U discharge E43075, $\rho = 0.95$. (*c*) The PNB+NNB phase of JT-60U discharge E43075, $\rho = 0.95$. The diagrams correspond to the magnetic surface with the maximum pressure gradient. The numbers on the plot indicate the toroidal mode numbers of the most unstable kink, peeling or ballooning mode. The solid curve marks the infinite n ballooning stability boundary, inside which the plasma is infinite n ballooning unstable. The dotted line marks the (sometimes assumed) finite n ballooning and/or kink/peeling stability boundaries. The operational point is marked with a dot.

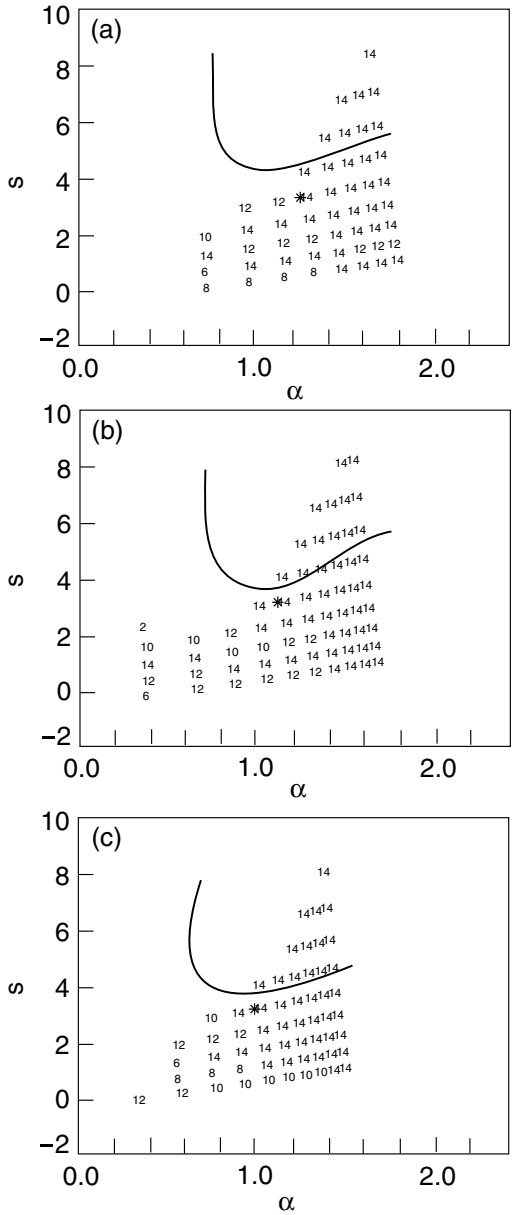

Figure 6. MHD stability diagrams illustrating the results of an aspect ratio scan, in which the aspect ratio of JET discharge 59219 has been varied artificially. (*a*) $\epsilon = 0.29$ (the actual inverse aspect ratio of the discharge). (*b*) $\epsilon = 0.27$ (*c*) $\epsilon = 0.25$ (approximately the JT-60U aspect ratio). The notation used in the diagrams is the same as figure 5.

In the dimensionless pedestal identity experiments, the levels of ripple at the outer midplane separatrix were of the order of 1% at JT-60U and 0.1% at JET. An important detail is that the ripple is much stronger with the JT-60U configuration not only at the outer midplane but also at the X-point. The fact that JET has 32 toroidal field coils with a unique capability to vary the current in every second coil makes it possible to carry out experiments with enhanced

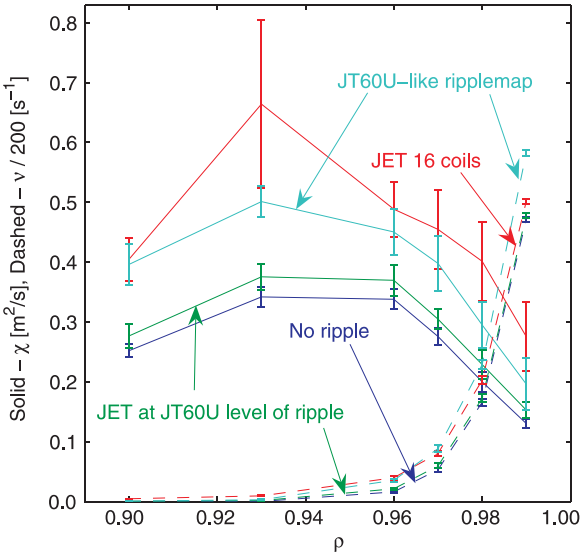

Figure 7. Collisional transport of thermal ions in JET discharge 60856 for a series of JET and JT-60U magnetic coil configurations as computed by ASCOT. The solid curves show the total ion thermal conductivity as a function of the radial co-ordinate for four different scenarios: the normal JET 32-coil configuration with the same current in both sets of coils ($I_1/I_2 = 1$, lowest curve), the JET coil configuration with the JT-60U level of ripple (1%) at the separatrix at the outer midplane, keeping the same on-axis toroidal field $B_t = 2.9$ T (second curve from the bottom), the JT-60U coil configuration (third curve from the bottom) and, finally, the JET coil configuration with only 16 coils ($I_1/I_2 = 0$), again keeping the same on-axis toroidal field (uppermost curve). The dashed curves show the ion escape rate due to non-diffusive losses in the same four simulations. The curve with the largest value at the separatrix corresponds to the JT-60U coil configuration. The effective charge Z_{eff} is 3.0 in these simulations.

toroidal magnetic field ripple at this machine. Back in 1995, when such experiments were carried out at JET, it was shown that a gradual increase in the ripple amplitude first leads to a modest improvement in plasma confinement, which is then followed by a degradation of the edge pedestal and finally by a transition to the L-mode regime, if the ripple amplitude increases above a certain level [19].

4. Orbit-following simulations

To begin with, the effect of ripple losses of thermal ions on ion thermal transport was studied in orbit-following simulations. The orbit-following Monte Carlo code ASCOT [20] was chosen as the numerical tool for studying the dependence of ripple-induced transport on the ripple amplitude and collisionality. In ASCOT, each test particle is followed along its guiding-centre orbit determined by the $\vec{E}_r \times \vec{B}$, polarization, gradient and curvature drifts and collisions. The ripple model in ASCOT [21] was updated to 3D, enabling more realistic estimates for the ripple losses to be obtained including the localization of the losses as a function of the ripple amplitude, plasma parameters and magnetic configuration. The JET and JT-60U magnetic configurations were used in the simulations. In the case of JET with the possibility of varying the current in every second of the 32 toroidal field coils from zero to maximum, the ripple field takes the form $B = B_0 + B_1 \cos(16\phi) + B_2 \cos(32\phi)$. Here, $B_1 \sim I_1 - I_2$ and $B_2 \sim I_1 + I_2$, where I_1 and I_2 are the currents in the odd- and even-numbered coils, respectively.

Two different techniques were used. In the first, more traditional method, the drift orbits of test particles with a Maxwellian distribution are followed. The test particles are seeded in the whole plasma volume according to the experimental background density profile. They maintain the background density profile in order to satisfy quasi-neutrality. The radial electric field is determined from the neo-classical radial current balance [21], from which follows that the radial ion current is zero. The advantage of this method is that it allows for quantitative evaluation of the total heat, particle and momentum losses across the separatrix as well as of the poloidal and toroidal distribution of these losses. The ion thermal conductivity χ_i is estimated from the heat flux evaluated from the particle ensemble [22]. As reported in [23], such simulations show a clear increase in heat transport and more locally distributed losses, when the current in every second coil is reduced in the JET configuration.

In the second method, the ion ensemble is initialized at a single flux surface with a Maxwellian velocity defined by the local temperature. The method allows for 'pulse spreading' simulations, i.e. the propagation of a heat and particle pulse across the magnetic field in the presence of toroidal magnetic field ripple can be studied. Local heat and particle transport coefficients can be deduced from simulations with this technique. The transport coefficients are measured from the variance growth of an initially radially localized test particle ensemble [23].

Figure 7 illustrates a characteristic result of the 'pulse spreading' simulations. Shown are the measured ion thermal conductivity and the ion escape rate plotted as a function of ρ for three simulations with the JET set of toroidal field coils and one with the JT-60U set of coils. The same background density, temperature and current profiles as well as the same on-axis toroidal field have been used in all simulations, but three different levels of magnetic ripple have been used with the JET configuration. In each case, toroidal magnetic field ripple has simply been added to the existing equilibrium without recalculating the equilibrium. The imposed ripple field is calculated from a system of current filaments grouped together to represent the toroidal field coils.

The first obvious conclusion from figure 7 is that ripple-induced transport can significantly exceed the level of ion neo-classical transport, provided that the ripple amplitude is large enough. Secondly, the figure also contains information highlighting the fact that there are two different mechanisms for losses of particles, both of which can be important. One mechanism arises from diffusive transport processes of the particles. In general, a transport equation for a general quantity A can be written as $\partial A/\partial t = \nabla \cdot (A\vec{v}) + \nabla \cdot (\mu \nabla A) + S$, where the first term represents convective transport, the second one diffusive transport and the third one sources and sinks. Here, $\vec{v}$ is the convective velocity and μ is a transport coefficient. Hereafter, ripple losses arising due to the transport processes represented by the diffusive term are referred to as losses due to diffusive transport. These losses can mainly be attributed to ripple well trapping, ripple-banana diffusion and neo-classical diffusion [24]. In high-collisionality plasmas, losses due to diffusive transport are dominant. A second loss mechanism is the direct escape of locally trapped particles due to vertical drift. These orbit losses, henceforth referred to as non-diffusive losses, correspond to the loss term S in the transport equation. They are mainly present in low-collisionality plasmas.

Indeed, the orbit-following simulations show that, depending on plasma collisionality, both losses due to diffusive transport and non-diffusive losses of thermal ions can be important. Figure 7 shows that in the case of diffusive losses, there is a wide region of enhanced transport extending significantly inside the pedestal. The toroidal distribution of losses turns out to be practically uniform. As shown by the ion escape rate graphs in the figure, the non-diffusive losses, on the contrary, are very edge-localized, affecting only the outer part of the ETB. The figure also shows that both the total ion thermal conductivity and the ion escape rate are higher with the JT-60U coil configuration than with the normal 32-coil JET configuration for the

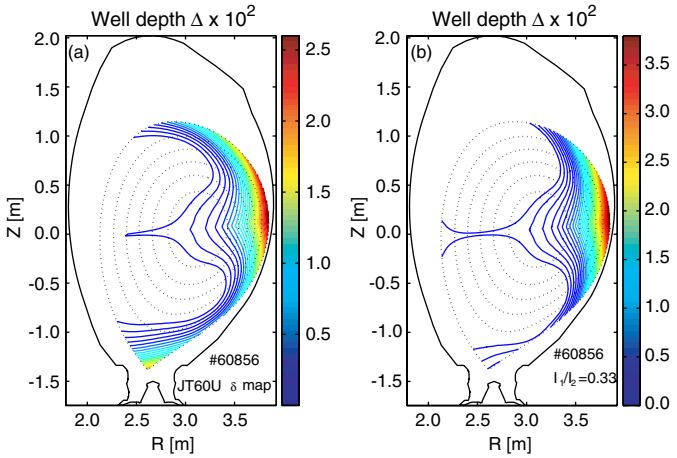

Figure 8. Contour plots of the maximum magnetic ripple well created by two different systems of toroidal field coils imposed on a JET equilibrium. Frame (*a*) corresponds to a situation with the JT-60U set of coils. Frame (*b*) corresponds to a situation with the JET set of coils with a ratio of the current in the first set of coils to the current in the second set of coils of 0.33 ($I_1/I_2 = 0.33$).

same level of ripple at the outer midplane. The radial extent of the losses is similar in both configurations. The level of ion thermal conductivity with the 16-coil JET configuration is comparable to or slightly larger than that with the JT-60U configuration.

Figure 8 shows two contour plots of the magnetic well created by two different systems of toroidal field coils imposed on a JET equilibrium, as described above. Frame (*a*) corresponds to a situation with the JT-60U coils, a set of 18 circular coils. Frame (*b*) corresponds to the situation with the JET set of D-shaped coils using a ratio of 0.33 for the currents in the two sets of coils ($I_2/I_1 = 0.33$). By comparing frames (*a*) and (*b*), it can be deduced that the same level of ripple at the outer midplane increases transport much less in the case of the JET magnetic configuration than in the case of the JT-60U-like configuration. This is due to the fact that JT-60U has circular coils, which produce a much stronger ripple near the X-point than the D-shaped JET coils. A strong ripple at the X-point means that the trajectory of an ion escaping there due to vertical drift is much shorter than that of an ion escaping from the outer midplane, which translates into more extensive non-diffusive losses. These losses may be an important reason for the differences in plasma performance between JET and JT-60U.

5. Predictive transport modelling of JET plasma with ripple losses

The results of the ASCOT orbit-following calculations were used as a basis for predictive transport modelling with the goal of simulating the dynamics of ELMy H-mode plasmas in the presence of ripple losses. Simple models (to be discussed in subsequent paragraphs) for losses due to diffusive transport and non-diffusive losses were implemented into the 1.5D core transport code JETTO [25] and used together with a mixed Bohm/gyro-Bohm transport model in code [26]. In JETTO, the ETB is represented by a sudden reduction in all transport coefficients to an ion neo-classical level in a typically 3–5 cm wide region at the edge of the plasma. For simplicity, the width of the ETB is considered a fixed parameter. The effect of letting the ETB width vary has been studied in [27].

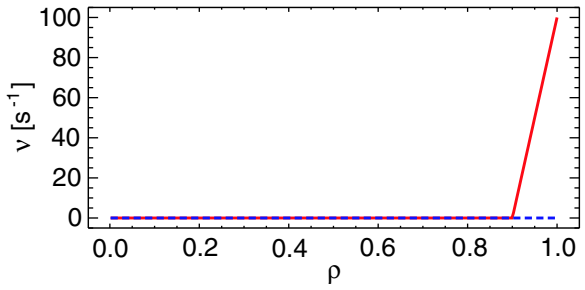

Figure 9. Radial profiles of the imposed ion escape rate in a simulation with the τ-approximation model for non-diffusive losses (——) and in a reference simulation with no imposed losses (- - - -).

ELMs have been modelled with a simple *ad hoc* model [28, 29]. When a fixed critical pressure gradient is exceeded somewhere within the pedestal, all transport coefficients are increased to pre-defined levels for a pre-defined duration of time in this region. In the simulations in this study, a critical pressure gradient of $\alpha = 1.28$ has been used. During the ELMs, ion and electron thermal transport within the ETB have been enhanced by a factor of 1000 and particle diffusivity by a factor of 50 for a duration of 1 ms, preceded and succeeded by short ramp-up and ramp-down times, respectively. In principle, the critical pressure gradient model applies only to ELMs driven by medium and high n ballooning-type modes, but it can be calibrated to indirectly take into account current-driven low n modes also by determining the pressure gradient limit with an MHD stability code such as MISHKA that treats all kinds of modes. For simplicity, and to allow for easy comparison, such recalibration of the critical pressure gradient for each individual simulation has, however, not been done in this study.

5.1. Modelling of the effects of non-diffusive losses

For non-diffusive losses of thermal ions, a simple *ad hoc* model commonly referred to as the τ-approximation was introduced by adding a convective term $-\nu n_\mathrm{i} T_\mathrm{i}$ to the continuity equation for the ion pressure:

$$\frac{\partial (n_\mathrm{i} T_\mathrm{i})}{\partial t} = P - \nabla(\chi_\mathrm{i} n_\mathrm{i} \nabla T_\mathrm{i}) - \frac{n_\mathrm{i} T_\mathrm{i}}{\tau_\mathrm{ripple}}. \tag{1}$$

Here, n_i is the ion density, T_i is the ion temperature, P is the power density, χ_i is the ion thermal conductivity and $\tau_\mathrm{ripple}(\rho) = 1/\nu(\rho)$ is the characteristic edge confinement time, which decreases strongly towards the separatrix due to non-diffusive losses.

Figures 9–11 illustrate the characteristic results obtained with the model for non-diffusive losses. Two simulations are used in each figure, one reference simulation with no non-diffusive losses and another one with a maximum loss rate of $\nu_\mathrm{max} = 100\,\mathrm{s}^{-1}$. In order to reflect the fact that non-diffusive losses are very edge-localized, the ion escape rate profile $\nu(\rho)$ has been kept zero throughout most of the core plasma and then ramped up linearly at the edge from $\rho = 0.90$. This is illustrated in figure 9, which shows the profile $\nu(\rho)$ in the two simulations. Figure 10, which shows the pressure profiles in the two simulations at times shortly before ELMs, illustrates the effect on plasma performance. By comparing the two graphs, it can be seen that there is a flattening of the pressure profile just inside the separatrix in the simulation modelling non-diffusive losses, which results in an effective narrowing of the pedestal. This effective narrowing of the pedestal leads to a lower top-of-the-pedestal pressure, which due to

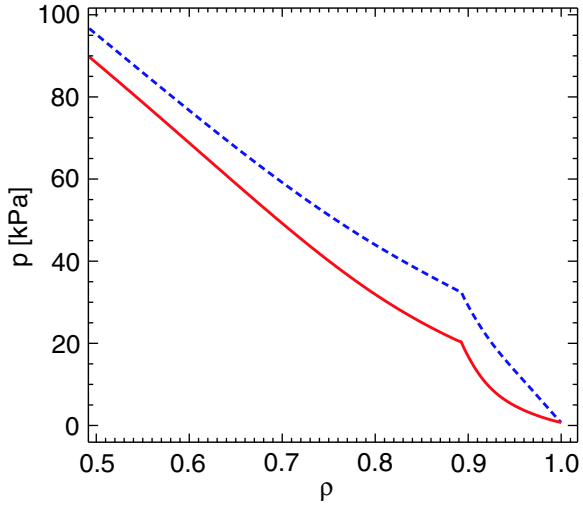

Figure 10. Radial profiles of the total pressure at times shortly before ELMs in the simulation with the τ-approximation model for non-diffusive losses (——) and in the reference simulation with no losses (- - - -).

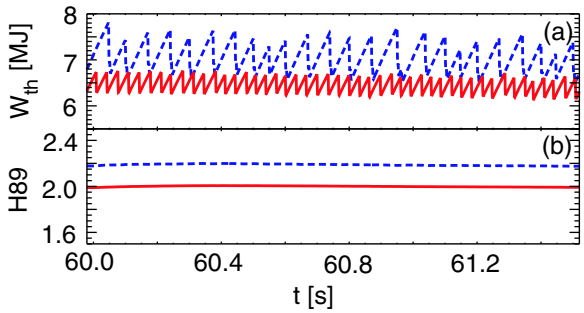

Figure 11. (*a*) Thermal energy content and (*b*) time-average confinement factor H-89 as a function of time in the simulation with the τ-approximation model for non-diffusive losses (——) and in the reference simulation with no losses (- - - -).

profile stiffness translates into lower pressure throughout the core plasma and thus into reduced confinement.

Here, it should be noted that the subject of profile stiffness, or the tendency of the relative temperature gradient $\nabla T/T$ to remain constant over large plasma regions, has been debated extensively [4, 30–36]. In general, the fulfilment of certain conditions seems to be necessary for the profiles to be stiff (e.g. $T_a > T_{\mathrm{gB}}$, $\chi_0 \ll \kappa_c \chi_{\mathrm{s}}$ according to [36], where T_a is the separatrix temperature, T_{gB} is a temperature determined from the heat flux at the separatrix with a gyro-Bohm scaling, χ_0 is the background thermal diffusivity, χ_{s} is a stiffness factor and $\kappa_c = -R\nabla T/T$ is a threshold for turbulent transport with R being the major radius and T the temperature). In the simulations in this study, profile-stiffness-like behaviour follows independently of the above criteria also from the $\chi_{\mathrm{B}} \sim |\nabla T/T_{\mathrm{tob}}|$ dependence of the Bohm term in the transport model, where χ_{B} is the Bohm contribution to the thermal diffusivity and T_{tob} is the temperature on the top of the ETB. It is also worth noting that the result of reduced

pedestal performance as a result of non-diffusive losses does not depend on the assumption of profile stiffness, which merely relates to overall confinement.

A further illustration of the effect on plasma performance is given in figure 11, which shows time traces of the thermal energy content and time-average confinement factor H-89 for the two simulations. The thermal energy content and the confinement factor decrease with increasing non-diffusive losses in accordance with the levels of plasma pressure in figure 10. The effect on the ELM frequency is visible in the traces of the thermal energy content in figure 11. The ELM frequency increases with increasing non-diffusive losses mainly because the ELM size drops due to the effective narrowing of the pedestal. With the effectively narrower pedestal and thus lower pedestal height, each ELM modelled by an increase in transport from the separatrix up to the top of the pedestal removes less energy and particles. The smaller ELM size for unchanged ELM amplitude and ELM duration with the introduction of non-diffusive losses is evident in figure 11. As a result of the smaller ELM energy and particle losses, the recovery from each ELMs is faster, whereby the ELM frequency goes up. Investigating how the ELM amplitude and duration may be affected by the ripple losses falls outside the scope of this first study, which aims to identify the most important qualitative trends. A second reason for the higher ELM frequency with the introduction of non-diffusive losses is the increased transport inside the pedestal. This follows from the profile-stiffness-like behaviour of the Bohm transport model in response to the lower pedestal height.

The reduced plasma confinement and increased ELM frequency obtained in the simulations with non-diffusive losses resemble the results obtained at JT-60U in the dimensionless pedestal identity experiments with JET. This suggests that non-diffusive losses associated with the stronger magnetic ripple at JT-60U might explain the modest pedestal performance and high ELM frequency observed in this machine. It should be noted that an inward movement of the top of the pedestal might weaken the tendency towards reduced confinement and higher ELM frequency observed in the simulations, but it is unknown whether ripple losses could at all have such an effect on the pedestal structure. Investigating how ripple losses may affect the pedestal width falls outside the scope of this study, which looks for qualitative trends from a transport point of view.

5.2. Modelling of the effects of losses due to diffusive transport

When modelling the effects of losses due to diffusive transport, a simple analytical approximation [24] for ripple-induced diffusive transport was introduced and suitably adjusted to the results of the ASCOT simulations (as described below). Scans over the width and amplitude of the additional ion thermal transport representing the ripple-induced contribution showed that such transport can have a profound impact on the severity of ELMs and confinement.

First, it was assumed that the ripple-induced ion thermal conductivity, in accordance with the orbit-following calculations, has a distribution with a characteristic width significantly wider than the pedestal width. Figures 12–16 illustrate a set of results obtained with this assumption. The radial profile of inter-ELM ion thermal conductivity used in the simulation is shown in figure 12 together with the profile from a reference simulation without additional transport. It should be noted that the transport perturbation is significant in amplitude well beyond the top of the pedestal in comparison with the ion neo-classical level of ion thermal conductivity within the ETB. Given the drop in background ion thermal conductivity at the top of the pedestal, this leads to the structure with two distinct peaks for the total ion thermal conductivity. The characteristic shape of the profile in the core plasma follows from the Bohm/gyro-Bohm transport model and varies somewhat over time.

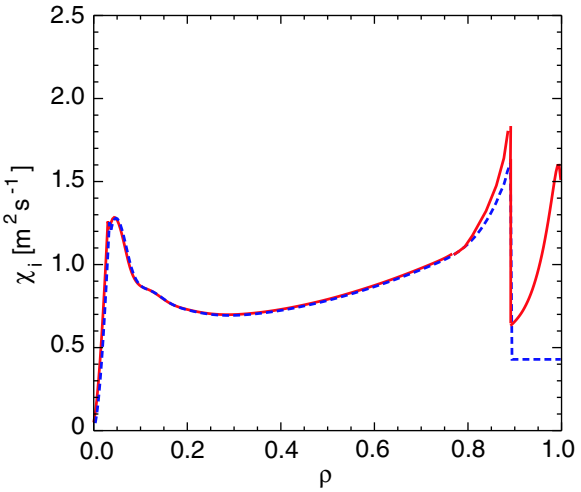

Figure 12. Radial profiles of ion thermal conductivity in two predictive transport simulations without (- - - -) and with (——) a contribution representing ripple-induced ion thermal transport at the edge. A broad radial profile consistent with the ASCOT simulations is assumed for the contribution representing ripple-induced transport.

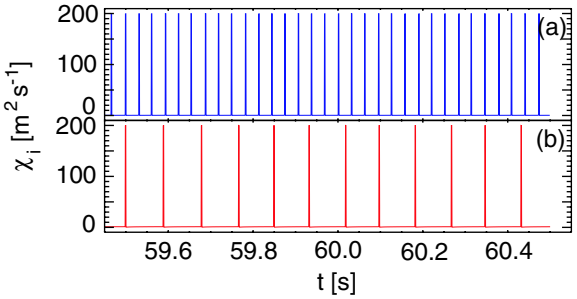

Figure 13. Ion thermal conductivity at $\rho = 0.95$ as a function of time in the two predictive transport simulations used in figure 12. (*a*) No contribution representing ripple-induced transport. (*b*) Ripple-induced transport included.

The effect on the ELM frequency of introducing the transport perturbations can be seen in figure 13, which shows the ion thermal conductivity at the magnetic surface $\rho = 0.95$ as a function of time. In this case, the ELM frequency decreases noticeably with the introduction of additional transport at the edge. The explanation for this is that the increased transport at the edge leads to increased losses between the ELMs and thus to a longer ELM build-up time. Here, this is the dominating mechanism affecting the ELM frequency. For clarity, it should be said that a similar tendency towards a lower ELM frequency is of course also present in the simulations of the effects of non-diffusive losses discussed in the preceding subsection, but there the mechanisms working towards a higher ELM frequency are much stronger and dominate the situation.

As a result of the lower ELM frequency with the introduction of ripple-induced transport, the time-average top-of-the-pedestal temperature increases considerably, even though the ultimate pre-ELM pedestal height does not change. The time-average temperature at the top of the pedestal is larger for a slower pedestal build-up, because the temperature generally increases most rapidly for a relatively constant amount of time right after an ELM crash

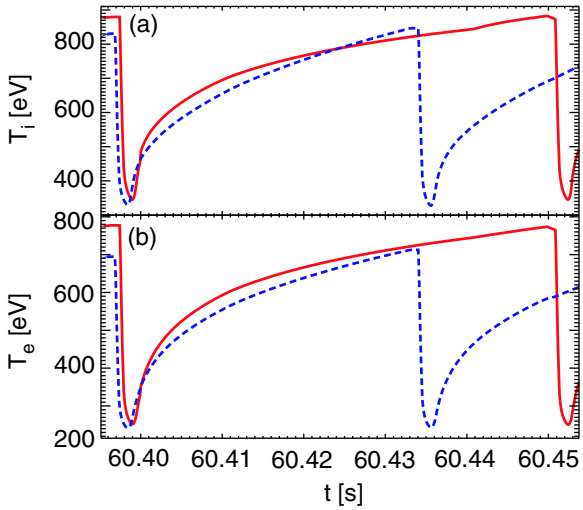

Figure 14. (*a*) Ion temperature and (*b*) electron temperature at the top of the pedestal as a function of time for the duration of the longer of the two ELM cycles in the two predictive transport simulations used in figure 12. - - - -: no contribution representing ripple-induced transport. ——: ripple-induced transport included.

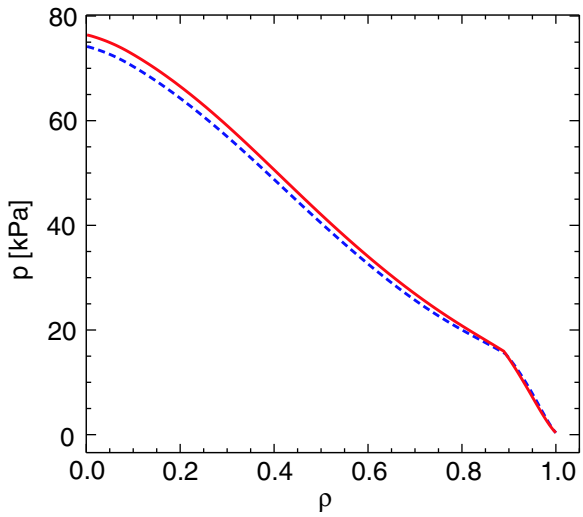

Figure 15. Radial profiles of the total pressure at times shortly before ELMs in the two predictive transport simulations used in figure 12. - - - -: no contribution representing ripple-induced transport. ——: ripple-induced transport included.

and then saturates more and more slowly over time before the next ELM. This is illustrated in figure 14, which shows the ion and electron temperatures at the top of the pedestal as a function of time for the duration of the longer of the two ELM cycles in the simulations with and without ripple-induced transport. It is evident that the time average of the ion and electron temperatures is higher in the case with lower ELM frequency. A demonstration of this effect is also provided by the limiting case of a stationary ELM-free H-mode, in which the pressure gradient saturates at a value just below the critical pressure gradient. In the absence of ELMs,

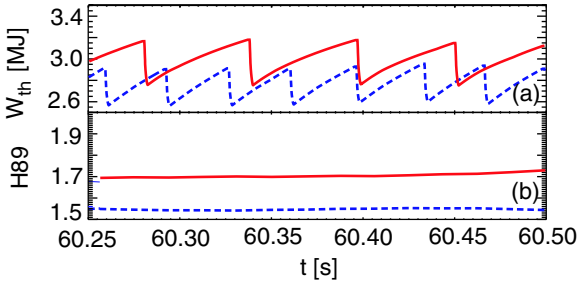

Figure 16. (*a*) Thermal energy content and (*b*) time-average confinement factor H-89 as a function of time in the two predictive transport simulations used in figure 12. - - - -: no contribution representing ripple-induced transport. ——: ripple-induced transport included.

the temperature at the top of the pedestal settles at a constant level almost as high as the pre-ELM temperature in an ELMy H-mode with the same critical pressure gradient. Clearly, the constant top-of-the-pedestal temperature in the ELM-free H-mode is above the time-average top-of-the-pedestal temperature in the ELMy H-mode.

The effect on plasma performance becomes evident in figure 15, which shows the pressure profiles in the simulations at times shortly before ELMs. The maximum pressure at the top of the pedestal is the same in the two cases, but since the lower ELM frequency in the simulation with ripple-induced transport leads to a higher time-average top-of-the-pedestal temperature and thus to a higher time-average top-of-the-pedestal pressure, the core pressure becomes higher in this case due to profile stiffness. In this way, ripple-induced additional ion thermal transport at the edge can lead to improved overall confinement. A further illustration of the improved performance resulting from the ripple-induced additional thermal conductivity is given in figure 16, which compares the thermal energy content and time-average confinement factor H-89 in the two simulations.

It should be noted that there are, in fact, some experimental indications of improved performance in the presence of ripple losses, as suggested by the modelling results. In particular, the improved performance demonstrated in the simulations qualitatively resembles the slight improvement in confinement obtained with small ripple amplitudes in previous JET experiments [19]. It should, however, be kept in mind that in this first study focusing on qualitative trends the ELM amplitude has been kept fixed. The tendency towards improved pedestal performance and less frequent ELMs may be reduced or strengthened, if the ELM amplitude changes due to the introduction of ripple losses. Investigating such effects is left for future work.

Finally, for a different set of simulations, it was assumed that the ripple-induced ion thermal conductivity is concentrated to a narrow region close to the separatrix with a characteristic width significantly narrower than the pedestal width. Such a profile has so far not been observed in the orbit-following simulations, but it is, nevertheless, interesting to consider what this assumption leads to in terms of plasma performance and ELM behaviour, because the results show how sensitively one type of behaviour changes into another type. A set of typical results obtained with this assumption is illustrated in figures 17–19. Figure 17 shows the inter-ELM ion thermal conductivity as a function of ρ in the simulation with ripple-induced ion thermal conductivity as well as in a reference simulation without additional transport. It should be noted that the amplitude of the ripple-induced transport perturbation is significant only in the outer half of the pedestal. At the top of the ETB, near $\rho = 0.9$, the perturbation is already very small.

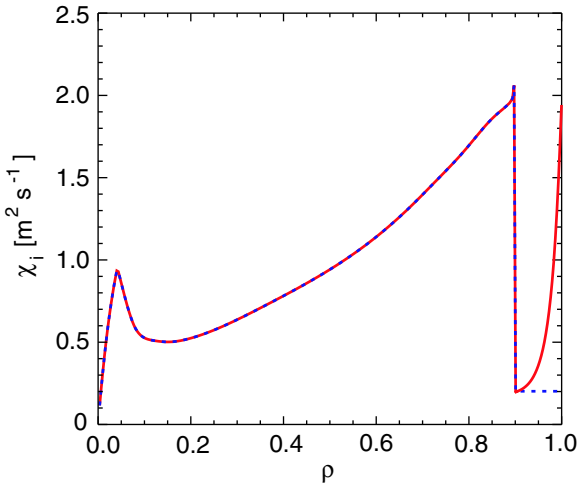

Figure 17. Radial profiles of ion thermal conductivity in two predictive transport simulations without (- - - -) and with (——) a contribution representing ripple-induced ion thermal transport at the edge. A narrow edge-localized profile is assumed for the contribution representing ripple-induced transport.

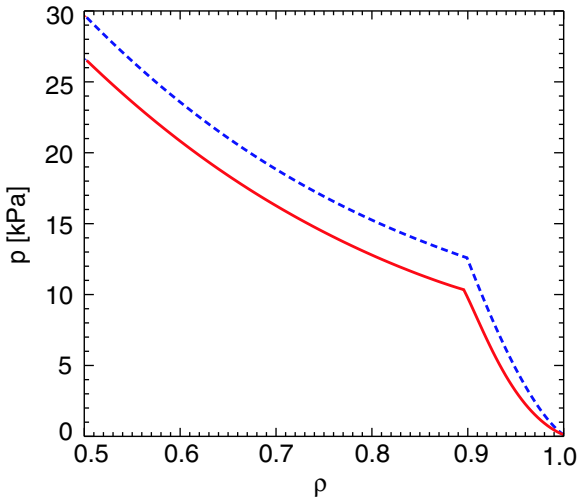

Figure 18. Radial profiles of the total pressure at times shortly before ELMs in the two predictive transport simulations used in figure 17. - - - -: no contribution representing ripple-induced transport. ——: ripple-induced transport included.

Not very surprisingly, the results obtained with a narrow region of enhanced ion thermal conductivity resemble those obtained with non-diffusive losses. The effect of the ripple-induced additional ion thermal conductivity on plasma performance is evident in figure 18, which shows the pressure profile in each simulation at a time shortly before an ELM. In the narrow region at the edge with enhanced transport, the pressure profile becomes almost flat due to large edge losses. This effective narrowing of the pedestal results in a lower pre-ELM pressure at the top of the pedestal in comparison with the unperturbed reference case.

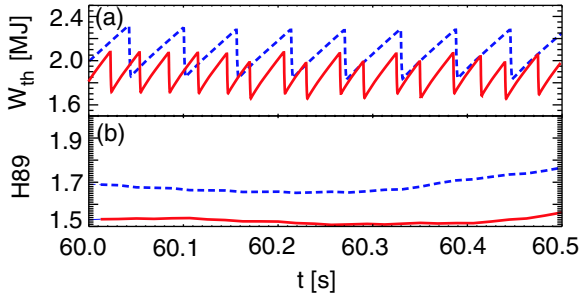

Figure 19. (*a*) Thermal energy content and (*b*) time-average confinement factor H-89 as a function of time in the transport simulations used in figure 17. - - - -: no contribution representing ripple-induced transport. ——: ripple-induced transport included.

Due to profile stiffness, the lower pedestal height translates into lower core pressure and thus reduced overall confinement. The larger the amplitude of the transport perturbation, the more pronounced is the effect. A further illustration of the reduced confinement due to ripple-induced ion thermal conductivity is provided in figure 19, which compares the thermal energy content and time-average confinement factor H-89 in the two simulations. Generally, a reduction in confinement is observed, if the additional transport due to losses of locally trapped thermal ions is mainly localized to the outer half of the pedestal. The ELM frequencies in the simulations used in figure 17 can be deduced from the time traces of the thermal energy content in frame (*a*) in figure 19. The ELM frequency increases with the introduction of ripple-induced transport mainly because the ELM size becomes smaller due to the effectively narrower pedestal, which leads to a shorter ELM build-up time.

6. Summary and discussion

The reasons for significant differences in pedestal performance and ELM frequency observed in a recent series of dimensionless pedestal identity experiments at JET and JT-60U have been investigated systematically. It has been shown that differences in the linear MHD stability of the pedestal do not explain the fact that the ELM frequency is higher and the pedestal performance lower at JT-60U. The mismatch in the aspect ratio between JET and JT-60U has been taken into account explicitly. A scan, in which the aspect ratio was varied and everything else kept constant, demonstrated that the aspect ratio has very little effect on the linear MHD stability of the pedestal. Taking toroidal rotation into account in the linear MHD stability analysis does not explain the observed discrepancies either, despite the fact that the rotation profiles were rather different at JET and JT-60U in the pedestal identity experiments. Given these findings, the influence of ripple-induced thermal ion losses on H-mode confinement, pedestal performance and ELM characteristics has been proposed as the main mechanism to explain the experimental results of the dimensionless pedestal identity experiments at JET and JT-60U.

The influence of ripple losses on ion thermal transport has been studied in orbit-following simulations. These simulations show that ripple-induced ion thermal transport can significantly exceed the level of ion neo-classical transport and thereby affect the physics of the H-mode pedestal. Depending on the collisionality, both losses due to diffusive transport and non-diffusive losses can be significant. In the case of losses due to diffusive transport, the region with enhanced ion thermal transport extends well beyond the top of the pedestal into the core, whereas, on the contrary, non-diffusive losses are very edge-localized.

The results of the orbit-following calculations have been applied in predictive transport simulations of ELMy H-mode plasmas. Most importantly, the transport simulations indicate that toroidal magnetic field ripple can influence ELM behaviour and plasma performance very sensitively. In the case of non-diffusive losses, the so-called τ-approximation has been used, in which a convective energy sink term is included into the continuity equation for the ion pressure. In these simulations, a deterioration of plasma confinement as well as an increase in the ELM frequency has been observed for a level of losses consistent with the orbit-following simulations. This result suggests that non-diffusive losses of thermal ions might play an important role in explaining the modest pedestal performance and the high ELM frequency characterizing JT-60U plasmas in the pedestal identity experiments with JET. The result also suggests that the toroidal magnetic field ripple could become an important tool for ELM mitigation. A similar result has been obtained by assuming a narrow edge-localized distribution of ion thermal transport induced by losses due to diffusive transport. It should, however, be noted that all the orbit-following simulations so far indicate that losses due to diffusive transport tend to have a rather broad radial distribution extending well beyond the top of the pedestal. In predictive transport simulations with additional ion thermal transport matching such a distribution of losses due to diffusive transport, an improvement in confinement and a reduction of the ELM frequency have been observed. Experimentally, a somewhat similar improvement in performance and reduction in ELM frequency was observed at the start of the H-mode phase, when the ripple amplitude was increased only slightly, in a series of experiments with enhanced toroidal magnetic field ripple at JET in 1995. A further increase in the ripple amplitude led to a deterioration of confinement and an increase in the ELM frequency, followed by a back H–L transition, which could suggest an interplay between the mechanisms described here.

It should be noted that fast ion losses may also play an important role in determining the pedestal physics. Recent experiments at JT-60U suggest that ripple-induced fast ion losses affect H-mode confinement, pedestal performance and ELM characteristics [12, 37], when a dominant part of the heating power comes from neutral beams with perpendicular injection. In order to separate the effects of ripple-induced fast and thermal ion losses and generally improve the understanding of the effects of ripple losses, scans in the ripple amplitude are foreseen as part of experimental campaigns devoted to studies of toroidal magnetic field ripple planned at both JET and JT-60U for 2006.

Above all, the results presented in this paper show that ripple losses of thermal ions seem to be a highly important effect influencing the performance of tokamak plasmas in different and often counter-intuitive ways. These results may have profound implications for the design of future tokamaks and in particular for ITER, which is planned to operate with an intermediate level of toroidal magnetic field ripple and for which large divertor heat loads are a concern. A particularly interesting result is that ripple losses need not necessarily have a detrimental influence on plasma performance. On the contrary, better overall confinement than in the absence of ripple could possibly be obtained by carefully choosing a suitable ripple amplitude profile. It should, however, be kept in mind that the models used in this study are relatively simple and could be improved in a number of ways. For instance, ripple-driven ion particle transport induces a radial electric field, which may affect the edge barrier. Ripple losses may also have an effect on the recycling of neutrals, which may again affect the pressure profile. In addition, magnetic ripple may have an influence on residual turbulent transport, which may also potentially modify the pedestal pressure. These effects, however, deserve separate investigation and fall outside the scope of this paper. Clearly, more work needs to be done in order for the subtle effects of ripple transport to be fully understood.

Acknowledgments

This work, supported by the European Communities under the contract of Association between EURATOM / Tekes, was carried out within the framework of the European Fusion Development Agreement. The views and opinions expressed herein do not necessarily reflect those of the European Commission.

Some of the computations presented in this document have been done in CSC's computing environment. CSC is the Finnish IT centre for science and is owned by the Ministry of Education.

References

[1] Connor J W 1998 *Plasma Phys. Control. Fusion* **40** 531
[2] Suttrop W 2000 *Plasma Phys. Control. Fusion* **42** A1
[3] Fundamenski V and Sipilä S 2004 *Nucl. Fusion* **44** 20
[4] Mikkelsen D R *et al* 2003 *Nucl. Fusion* **43** 30
[5] ITER Physics Expert Group on Confinement *et al* 1999 *Nucl. Fusion* **39** 2175
[6] Cordey J G 2003 *Nucl. Fusion* **43** 670
[7] McDonald D *et al* 2007 *Nucl. Fusion* **47** at press
[8] Saibene G *et al* 2004 *Plasma Phys. Control. Fusion* **46** A195
[9] Sakamoto Y *et al* 2004 *Nucl. Fusion* **44** 876
[10] Mikhailovskii A B *et al* 1997 *Plasma Phys. Rep.* **23** 844
[11] Chapman I T, Sharapov S E, Huysmans G T A and Mikhailovskii A B 2006 *Phys. Plasmas* **13** 062511
[12] Urano H *et al* 2006 *Plasma Phys. Control. Fusion* **48** A193
[13] Oyama N *et al* 2005 *Nucl. Fusion* **45** 871
[14] Tobita K *et al* 1992 *Phys. Rev. Lett.* **69** 3060
[15] Tobita K *et al* 1995 *Nucl. Fusion* **35** 1585
[16] Sadler G *et al* 1992 *Plasma Phys. Control. Fusion* **34** 1971
[17] Putvinskij S V *et al* 1994 *Nucl. Fusion* **34** 495
[18] Shinohara K *et al* 2003 *Nucl. Fusion* **43** 586
[19] Tubbing B 1995 *Proc. 22nd European Physical Society Conf. on Controlled Fusion and Plasma Physics (Bournemouth, UK)* vol 19C (ECA) part IV, p IV-001
[20] Kurki-Suonio T *et al* 2002 *Nucl. Fusion* **42** 725
[21] Heikkinen J A *et al* 2001 *J. Comput. Phys.* **173** 527
[22] Kiviniemi T P *et al* 2002 *Contrib. Plasma Phys.* **42** 236
[23] Kiviniemi T P *et al* 2005 *Proc. 32nd European Physical Society Conf. on Plasma Physics (Tarragona, Spain)*
[24] Yushmanov P N 1991 *Review of Plasma Physics* vol 16 (New York: Consultants Bureau)
[25] Cennachi G and Taroni A 1988 *JET-IR(88) 03*
[26] Erba M *et al* 1997 *Plasma Phys. Control. Fusion* **39** 261
[27] Onjun T, Bateman G, Kritz A H and Hammett G 2002 *Phys. Plasmas* **9** 5018
[28] Lönnroth J-S *et al* 2003 *Plasma Phys. Control. Fusion* **45** 1689
[29] Lönnroth J-S *et al* 2004 *Plasma Phys. Control. Fusion* **46** 767
[30] Coppi B and Sharky N 1981 *Nucl. Fusion* **21** 1363
[31] Ryter F *et al* 2001 *Phys. Rev. Lett.* **86** 2325
[32] Hoang G T *et al* 2001 *Phys. Rev. Lett.* **87** 125001
[33] Baker D R *et al* 2001 *Phys. Plasmas* **8** 4128
[34] Mantica P *et al* 2002 *Plasma Phys. Control. Fusion* **44** 2185
[35] Peeters A G 2002 *Nucl. Fusion* **42** 1376
[36] Garbet X *et al* 2004 *Plasma Phys. Control. Fusion* **46** 1351
[37] Kamiya K *et al* 2006 *Plasma Phys. Control. Fusion.* **48** A131